Impact of Nanostructure Configuration on the Photovoltaic Performance of Quantum-Dot Arrays

Aude Berbezier and Urs Aeberhard*

IEK5-Photovoltaik, Forschungszentrum Jülich, 52425 Jülich, Germany

(Received 11 August 2015; published 19 October 2015)

In this paper, a mesoscopic model based on the nonequilibrium Green's function formalism for a tight-binding-like effective Hamiltonian is used to investigate a selectively contacted quantum-dot array designed for operation as a single-junction quantum-dot solar cell. By establishing a direct relation between nanostructure configuration and optoelectronic properties, the investigation reveals the influence of interdot and dot-contact coupling strengths on the rates of charge-carrier photogeneration, radiative recombination, and extraction at contacts, and, consequently, on the ultimate performance of photovoltaic devices with finite quantum-dot arrays as the active medium. For long carrier lifetimes, the dominant configuration effects originate in the dependence of the joint density of states on the interdot coupling in terms of band width and effective band gap. In the low-carrier-lifetime regime, where recombination competes with carrier extraction, the extraction efficiency shows a critical dependence on the dot-contact coupling.

DOI: 10.1103/PhysRevApplied.4.044008

I. INTRODUCTION

In a large variety of concepts for next-generation solar cells, such as devices based on intermediate bands, hot carriers, or multiple exciton generation, nanostructures like quantum wells, wires, or dots provide the specific physical properties required to reach beyond current efficiency limitations [1–3]. Among these nanostructures, quantum dots (QDs) are of special interest due to their largely tunable optoelectronic characteristics, and regimented QD structures, thus, represent promising candidates for the implementation of high-efficiency solar-cell concepts [4–9].

However, to enable exploitation of the design degrees of freedom provided, the complex relation between structural configuration parameters and device characteristics requires thorough investigation. In conventional detailed-balance modeling approaches, this connection is provided only indirectly via the local variation of macroscopic bulk material parameters such as the absorption coefficient, mobility, and lifetime of charge carriers [10–12]. For a direct, consistent, and comprehensive assessment of configuration-related photovoltaic performance, both interband dynamics and transport of charge carriers need to be described in a unified microscopic picture, like the one provided by the nonequilibrium Green's function (NEGF) formalism [13]. Since a fully microscopic treatment of extended systems of coupled QDs comes with a huge computational cost, application of multiscale approaches is required, such as the mesoscopic QD orbital tight-binding model introduced in Ref. [14].

Here, this model is used in a simplified version, with restriction to a single basis orbital per band, phenomenological nearest-neighbor hopping parameters, and flat-band conditions. These simplifications assure maximum transparency in the analysis of the photovoltaic mechanisms in the QD arrays considered and allow for direct comparison with the conventionally used periodic picture of an infinite QD chain. In this way, clear relations can be established between the radiative limit of photovoltaic device performance and configuration-dependent properties such as the finite system size in terms of a limited number of QD layers, the coupling between QDs, and the presence and nature of contacts.

While the restriction to single QD arrays, lowest minibands, and flat potential does not allow for a direct application to real-world QD solar-cell devices, the general approach and qualitative analysis presented below is essentially transferable to those more complex systems. Of these devices, the single-QD arrays can still be viewed as the main building blocks, with photovoltaic characteristics as determined here.

The article is organized as follows. In Sec. II, the model for the electronic structure and the dynamics of charge carriers in selectively contacted quantum-dot arrays under illumination is discussed in detail. The focus is on properties relevant for photovoltaic device operation, such as absorption cross section, emission spectra, and carrier extraction efficiency. In Sec. III, the numerical implementation of the model is evaluated for a range of interdot and dot-contact coupling values for both long and short charge-carrier lifetimes. The results are briefly summarized in the last section.

II. MODEL

A. Hamiltonian and NEGF equations

The phenomenological Hamiltonian for the device sketched in Fig. 1 reads ($b \in \{c, v\}$),

*u.aeberhard@fz-juelich.de

$$\hat{\mathcal{H}}_0^b = \sum_{i=1}^{N_{\mathrm{QD}}-1} t_{b,ii+1}[\hat{d}_{b,i+1}^\dagger \hat{d}_{b,i} + \mathrm{H.c.}] + \sum_{i=1}^{N_{\mathrm{QD}}} \varepsilon_{b,i}\hat{n}_{b,i} \quad (1)$$

$$\equiv \sum_{i,j=1}^{N_{\mathrm{QD}}} H_{0,ij}^b \hat{d}_{b,i}^\dagger \hat{d}_{b,j}, \quad (2)$$

where N_{QD} is the number of dots, t_b is the interdot coupling, $\hat{n}_b \equiv \hat{d}_b^\dagger \hat{d}_b$ is the carrier density operator, and ε_b is the QD energy level. The phenomenological parameters can, in principle, be determined from a microscopic theory of the QD states for a given nanostructure configuration, e.g., via QD Wannier functions [15], but this is beyond the scope of the present paper. Here, we will concentrate on the impact of the magnitude of these parameters on the optoelectronic properties that are relevant for the photovoltaic performance. An estimate for a realistic range of interdot coupling strengths can be obtained, e.g., from the coefficients of a cosine Fourier expansion of the dispersion relation for superlattice Bloch states [16]. Here, we consider values in the intermediate- to strong-coupling regime, corresponding to closely spaced QDs, which is the preferred situation for photovoltaic applications relying on miniband transport.

The Hamiltonian in Eq. (1) is used in the equations for the steady-state charge-carrier NEGF, which read for a given band and energy E:

$$\mathbf{G}^R(E) = [\{\mathbf{G}_0^R(E)\}^{-1} - \Sigma^{RI}(E) - \Sigma^{RB}(E)]^{-1}, \quad (3)$$

$$\mathbf{G}^\lessgtr(E) = \mathbf{G}^R(E)[\Sigma^{\lessgtr I}(E) + \Sigma^{\lessgtr B}(E)]\mathbf{G}^A(E), \quad (4)$$

where

$$\mathbf{G}_0^R(E) = [(E+i\eta)\mathbb{1} - \mathbf{H}_0]^{-1}, \mathbf{G}^A = [\mathbf{G}^R]^\dagger, \quad (5)$$

and $\mathbf{G} \equiv [G_{ij}]$ with

$$G_{ij}(E) = \int d\tau e^{iE\tau/\hbar} G_{ij}(\tau), \qquad \tau = t' - t, \quad (6)$$

and

$$G_{ij}(t,t') = -\frac{i}{\hbar}\langle \hat{T}_C\{\hat{d}_i(t)\hat{d}_j^\dagger(t')\}\rangle \quad (7)$$

is the ensemble average ordered on the Keldysh contour [17]. Equations (3) and (4) are solved self-consistently with the expressions for the interaction self-energy terms $\Sigma^{\cdot I}$, which include the interactions relevant for the photovoltaic device operation, i.e., coupling to photons, phonons, and to other charge carriers (not considered in this work).

The self-energy (SE) terms $\Sigma^{\cdot B}$ encode the hybridization of QD and contact states, enabling the description of charge-carrier extraction and injection at the electrodes:

$$\Sigma_{ij}^{RB}(E) = \delta_{ij}\left[\Delta_B(E) - \frac{i}{2}\Gamma_B(E)\right], \quad (8)$$

$$\Sigma_{ij}^{\lessgtr B}(E) = i\left[f(E-\mu_B) - \frac{1}{2} \pm \frac{1}{2}\right]\delta_{ij}\Gamma(E), \quad (9)$$

where $B \in \{L, R\}$, f is the Fermi-Dirac distribution function, and μ_B is the chemical potential of the contact considered. The real part Δ_B describes the energetic shift of the electronic states due to coupling to the electrodes, and the broadening function Γ_B is related to the coupling parameter V_B and to the local density of states (LDOS) ρ_B of the electrode contact layer through $\Gamma_B(E) = 2\pi V_B^2 \rho_B(E)$. In this paper, the semi-infinite 1D tight-binding chain description of a finite band-width electrode is used [18], with

$$\Delta_B(E) = \frac{\Gamma_0}{2} \times \begin{cases} x, & |x| \le 1, \\ \left(x - \mathrm{sgn}(x)\sqrt{x^2-1}\right), & |x| > 1, \end{cases} \quad (10)$$

$$\Gamma_B(E) = \Gamma_0 \theta(1-|x|)\sqrt{1-x^2}, \quad (11)$$

$$\Gamma_0 = 2V_B^2/|t_B|, \qquad x = (E-\varepsilon_B)/(2|t_B|), \quad (12)$$

where ε_B is the on-site energy and t_B the hopping element of the electrode material. In order to enable efficient charge-carrier injection and extraction, overlap of electrode and QD DOS demands $\varepsilon_B' \equiv \varepsilon_B - 2|t_B| < \varepsilon_b - 2|t_b|$ (electron case).

For the numerical example, we chose $\{\varepsilon_v, \varepsilon_c\} = \{-0.7, 0.6\}$ eV, similar to the values obtained for the lowest states of PbSe colloidal QDs of approximately 3 nm diameter using $\mathbf{k}\cdot\mathbf{p}$ band-structure calculations [19–21]. The determination of the magnitude of the coupling constant V_B usually requires a full microscopic treatment of the contact region. An estimate of the relevant range of coupling values can be obtained from the comparison of the LDOS and density from full solution of the Schrödinger equation in this region with the same quantities as obtained by the phenomenological approach above for different values of V_B. In order to achieve the carrier selectivity required for charge separation and current rectification in the absence of a built-in potential, the contact couplings are set to zero at the minority carrier boundaries, which are chosen at the left electrode for electrons and at the right electrode for holes, i.e., $V_{cL} = V_{vR} = 0$ (see, also, Fig. 1). For the electrode states, $\{\varepsilon_{vL}, \varepsilon_{cR}\} = \{-0.6, 0.5\}$ and $|t_B| = \hbar^2/(2m_B^*\Delta^2)$ for $B \in \{vL, cR\}$, with $m_B^* = 0.25m_0$ and $\Delta = 2.7$ Å are used.

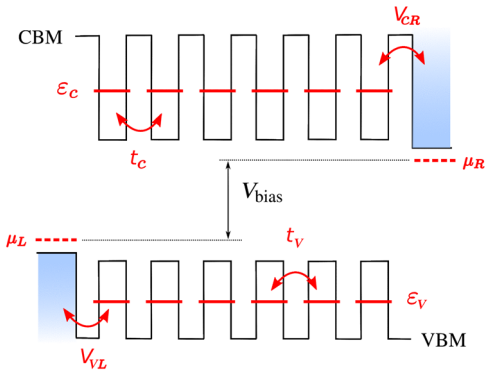

FIG. 1. Schematic band diagram and phenomenological parameters characterizing the selectively contacted QD array. Isolated QD states at energies $\varepsilon_{c,v}$ are connected through interdot coupling terms $t_{c,v}$. To enable photocarrier extraction and injection of dark current under applied bias voltage $V_{\rm bias}$, the QD states are connected to contacts via coupling elements V_B. The carrier selectivity of the contacts, i.e., $V_{cL} = V_{vR} = 0$, is required for photocurrent rectification at flat-band conditions in the absence of a doping-induced junction. While left and right contacts are assumed to be equilibrated with charge-carrier populations characterized by chemical potentials μ_L and $\mu_R = \mu_L + V_{\rm bias}$, respectively, the carrier population inside the absorber emerges entirely from the quantum-statistical formalism applied.

B. Density of states

At this level, i.e., without consideration of the interaction processes, the formalism provides the electronic structure of the noninteracting system under arbitrary nonequilibrium conditions, e.g., via the local density of charge-carrier states $\rho_i(E) = -(1/\pi)\mathrm{Im}G^R_{ii}(E)$, where i labels the dot position. Figure 2 displays the LDOS for an array of 20 coupled QDs, together with the total DOS obtained from summing the individual QD contributions. In contrast to standard simulations of QD-based solar cells, where extended QD superlattices are modeled using periodic boundary conditions [22,23], discrete states can still be distinguished in the total DOS. On the other hand, the main effect of the presence of a contact is the broadening and shifting of the LDOS according to the electrode DOS (dashed lines), especially in the vicinity of the electrode, where the band width is strongly increased from the limiting value of $\sim 4|t_b|$ $(b = c, v)$ of the infinite single-orbital tight-binding (TB) chain (dotted horizontal lines). This limiting value is nearly recovered in arrays with as few as 20 QDs. The energy integration of the total DOS yields $N_{\rm QD}$, in agreement with the associated sum rule. The effects of finite system size persist up to a large number of QDs, as can be verified in Fig. 3 displaying the convergence of the average electron DOS per QD with increasing number of QDs towards the infinite 1D TB chain limit given by

$$\bar{\rho}_{c,\infty}(E) = \left[2\pi|t_c|\sqrt{1-\left(\frac{E+i\eta_c-\varepsilon_c}{2|t_c|}\right)^2}\right]^{-1}, \qquad (13)$$

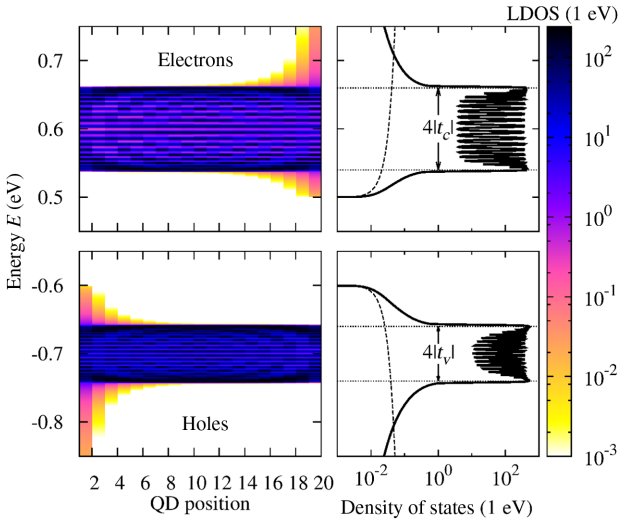

FIG. 2. Local (left) and total (right) density of electron and hole states for a selectively contacted 20-QD array with $V_{cR} = V_{vL} = 0.1$ eV, $t_c = -0.03$ eV, and $t_v = -0.02$ eV. At the closed contacts, the band width approaches the infinite single-orbital tight-binding chain value of $4|t_b|$, $b = c, v$ (dotted lines). On the contrary, at the open contacts, hybridization with contact states induces a pronounced widening of the bands and a shift of the band edge towards the electrode edges at $\varepsilon'_{cR} = 0.5$ eV and $\varepsilon'_{vL} = -0.6$ eV, according to the local density of contact states at the surface of the semi-infinite electrode (dashed lines).

for which a homogeneous broadening of $\eta_c = 0.5$ meV is assumed. Thus, while the band width of the finite system is almost identical to that of the infinite chain, the spectral distribution of the DOS differs considerably even for moderate QD numbers, from clearly distinguishable contributions of individual dots to a smooth continuum.

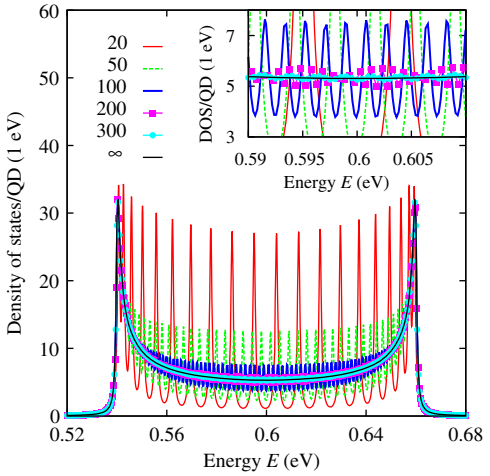

FIG. 3. Convergence of the average density of electronic states per QD to the infinite 1D TB chain limit with increasing number of QDs between the contacts, assuming symmetric contact coupling $V_{cL} = V_{cR} = 0.1$ eV, $t_c = -0.03$ eV, and a homogeneous broadening $\eta_c = 0.5$ meV.

Since photovoltaic devices are operated at or above room temperature, thermal broadening is considered via the physical line shape provided by quasielastic coupling to phonons. Indeed, at the coherent limit, the weak interdot and dot-contact coupling and resulting strong localization of charge carriers on the QDs will lead to extremely sharp resonances in the spectral quantities, exhibiting line widths far below the thermal energy at room temperature. For the computation of static spectral quantities such as the electronic density of states, a homogeneous broadening can be introduced via the damping parameter η. However, this is not a valid approach for transport simulations, as it violates current conservation [24]. Therefore, for the evaluation of transport properties, broadening induced by scattering of charge carriers and optical phonons is considered on the level of the current-conserving self-consistent Born approximation for the coupling of interacting fermions to a noninteracting phonon bath [25]. Since at this stage, no real phonon modes are considered, a constant effective coupling matrix element $|\bar{\mathcal{M}}_{\rm ph}|^2 \approx 1$ meV diagonal in the electronic indices, and a phonon frequency $\hbar\Omega \approx$ 0.2–0.5 meV is assumed, which provides a quasielastic scattering resulting in a local inhomogeneous broadening. The corresponding self-energies have the form

$$\Sigma^{\lessgtr}(E) = |\bar{\mathcal{M}}_{\rm ph}|^2[N_{\rm ph}\mathbf{G}^{\lessgtr}(E \mp \hbar\Omega) + (N_{\rm ph}+1)\mathbf{G}^{\lessgtr}(E \pm \hbar\Omega)], \tag{14}$$

$$\Sigma^{R}(E) = |\bar{\mathcal{M}}_{\rm ph}|^2[(N_{\rm ph}+1)\mathbf{G}^{R}(E-\hbar\Omega) + N_{\rm ph}\mathbf{G}^{R}(E+\hbar\Omega) + \frac{1}{2}\{\mathbf{G}^{<}(E+\hbar\Omega) - \mathbf{G}^{<}(E-\hbar\Omega)\}], \tag{15}$$

where the phonon-mode occupation number is given by the Bose-Einstein function $N_{\rm ph} = (e^{\hbar\Omega/k_BT}-1)^{-1}$. Figure 4 displays the integrated density of states for different broadening mechanisms, i.e., for broadening induced by interdot and dot-contact coupling only (coh), for homogeneous broadening with $\eta = 0.5$ meV (hom), and for quasielastic coupling to optical phonons of energy $\hbar\Omega =$ 0.2 meV (phon).

C. Absorption and photocurrent generation

In the coupling of charge carriers to electromagnetic fields, stimulated and spontaneous processes need to be distinguished. Photogeneration and stimulated emission induced by incident radiation is described via the self-energy for the interaction with a classical field with vector potential $\mathbf{A}$ [26]

$$\Sigma^{e\gamma-st,\lessgtr}_{ij,\eta}(E,\hbar\omega) = \mathcal{M}^{e\gamma,\eta}_i\mathcal{M}^{e\gamma,\eta}_j\{G^{\lessgtr}_{ij}(E-\hbar\omega) + G^{\lessgtr}_{ij}(E+\hbar\omega)\}A_\eta(\mathbf{R}_i,\hbar\omega)A_\eta(\mathbf{R}_j,\hbar\omega), \tag{16}$$

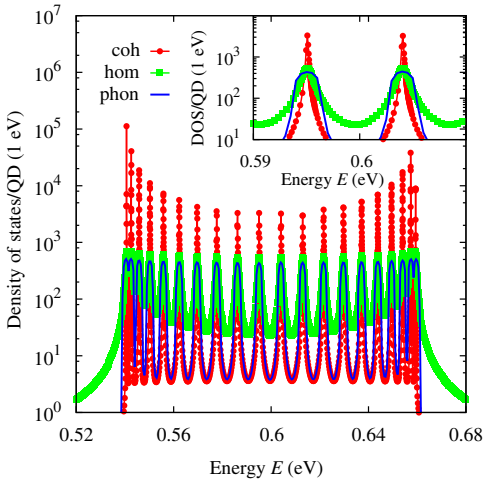

FIG. 4. Site-integrated density of electron states for a 20-QD array ($V_{cL} = V_{cR} = 0.1$ eV, $t_c = -0.03$ eV) with coupling-induced broadening only ("coh"), constant homogeneous broadening $\eta = 0.5$ meV ("hom"), and for quasielastic coupling to optical phonons of energy $\hbar\Omega = 0.2$ meV ("phon").

$$\Sigma^{e\gamma-st,R} \approx \frac{1}{2}(\Sigma^{e\gamma-st,>} - \Sigma^{e\gamma-st,<}), \tag{17}$$

with $\hbar\omega$ the photon energy, $\eta \in \{x,y,z\}$ the polarization component, and the coupling matrix elements $\mathcal{M}^{e\gamma,\eta}_i \equiv -(e/m_0)p^{\eta}_{cv}(\mathbf{R}_i)$, where p_{cv} is the interband momentum matrix element and $\mathbf{R}_i$ the QD position. For electrons, the first term in curly brackets provides the generation, while the second term yields the stimulated emission. The attenuation of the electromagnetic field relates to the absorption cross section (AC) $\mathcal{A}$ of the QD array via the absorption coefficient $\alpha(\hbar\omega) = \rho_{\rm QD}\mathcal{A}(\hbar\omega)$, where $\rho_{\rm QD}$ is the QD density. For a single-QD array or a very dilute QD system, the attenuation of the incident field can be neglected. The AC itself is computed based on the electronic structure from the net spectral absorption rate and the incident photon flux via $\mathcal{A}_\eta(\hbar\omega) \equiv \mathcal{R}^{\eta}_{\rm abs,net}(\hbar\omega)/\Phi^{\gamma}_{0\eta}(\hbar\omega)$, with

$$\mathcal{R}^{\eta}_{\rm abs,net}(\hbar\omega) = \int\frac{dE}{2\pi\hbar}\sum_{i,j}[G^{>}_{ij}(E)\Sigma^{e\gamma-st,<}_{ji}(E,\hbar\omega) - G^{<}_{ij}(E)\Sigma^{e\gamma-st,>}_{ji}(E,\hbar\omega)], \tag{18}$$

and $\Phi^{\gamma}_{0\eta}(\hbar\omega) = 2n_rc_0\varepsilon_0\hbar^{-1}\omega|A_\eta(\mathbf{R}_0,\hbar\omega)|^2$, where a background refractive index n_r is assumed, which for the numerical evaluations is set to $n_r = 3.63$. Using the above expressions for absorption rate and photon flux yields the following expression for the AC in terms of the photon self-energy Π:

$$\mathcal{A}_\eta(\hbar\omega) = \frac{c_0}{2n_r\omega}\sum_{i,j}\mathrm{Re}\{i\hat{\Pi}_{ji,\eta\eta}(\hbar\omega)\}. \quad (19)$$

Expression (19) considers the net absorptance, i.e., including stimulated emission, by the definition of $\hat{\Pi} \equiv \Pi^> - \Pi^<$ from the photon SE components:

$$\Pi^{\lessgtr}_{ij,\eta\eta'}(E) = -i\hbar\mu_0\mathcal{M}_i^{e\gamma,\eta}\mathcal{M}_j^{e\gamma,\eta'}\mathcal{P}^{\lessgtr}_{ij}(E), \quad (20)$$

where the electron-hole polarization function elements are

$$\mathcal{P}^{\lessgtr}_{nm}(E) = \int\frac{dE'}{2\pi\hbar}G^{\lessgtr}_{nm}(E')G^{\gtrless}_{mn}(E'-E), \quad (21)$$

and which is, hence, related to the spectral function $\hbar\hat{\mathcal{P}}/2\pi$ of occupied electron-hole pairs ($\hat{\mathcal{P}} \equiv \mathcal{P}^> - \mathcal{P}^<$) [27]. At global quasiequilibrium conditions, where the carrier populations are fixed by global quasi-Fermi-levels (QFLs) μ_b ($b = c, v$), the fluctuation-dissipation theorem provides the relations

$$\mathbf{G}^{\lessgtr}_b(E) = i\hat{\mathbf{G}}_b(E)[f(E-\mu_b) - 1/2 \pm 1/2], \quad (22)$$

where

$$\hat{\mathbf{G}} \equiv i(\mathbf{G}^> - \mathbf{G}^<) = i(\mathbf{G}^R - \mathbf{G}^{R,\dagger}) = -2\mathrm{Im}\mathbf{G}^R \quad (23)$$

are the spectral functions of the charge carriers. Far away from degeneracy and under low-intensity excitation, band-filling effects can be neglected, and the electron-hole spectral function is proportional to the joint density of states (JDOS) of the system, which, in turn, can be written in terms of the spectral functions of the individual charge carriers as follows:

$$\mathcal{J}_{cv}(E) = \int\frac{dE'}{4\pi^2}\mathrm{tr}\{\hat{\mathbf{G}}_c(E')\hat{\mathbf{G}}_v(E'-E)\} \quad (24)$$

$$\equiv\sum_i\mathcal{J}_{cv,i}(E), \quad (25)$$

defining the local joint density of states (LJDOS) as

$$\mathcal{J}_{cv,i}(E) = \int\frac{dE'}{4\pi^2}\sum_k\hat{G}_{c,ik}(E')\hat{G}_{v,ki}(E'-E) \quad (26)$$

$$\equiv\sum_k\mathcal{J}_{cv,ik}(E). \quad (27)$$

While the LJDOS is directly related to the local absorption coefficient, the last expression defines the contributions to the (L)JDOS according to nonlocality, i.e., according to the extent of spatially off-diagonal elements of the carrier Green's functions considered in Eq. (27). Figure 5 shows the evolution of the JDOS with increasing degree of nonlocality: while, remarkably, the sum rule is observed in all cases, the JDOS deviates strongly from the full result for restricted nonlocality, as observed previously for other nanosystems [28,29]. As for the DOS, the JDOS converges with increasing number of QDs to that of the infinite tight-binding chain for two coupled single-orbital bands. This is displayed in the inset of Fig. 5, where the JDOS provided by the NEGF formalism for a system of 300 coupled and selectively contacted QD (open circles) is shown together with the result for the infinite 1D TB chain (solid line), which in complete analogy to Eq. (13) reads

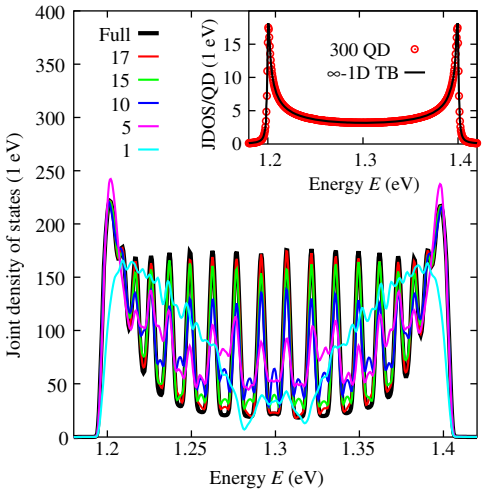

FIG. 5. Convergence of the JDOS of a 20-QD system with increasing nonlocality and to the infinite 1D TB chain for large system size (inset).

$$\mathcal{J}_{cv,\infty}(E) = \left[2\pi t_{cv}\sqrt{1-\left(\frac{E+i\eta_{cv}-\varepsilon_{cv}}{2t_{cv}}\right)^2}\right]^{-1}, \quad (28)$$

where $t_{cv} = |t_c| + |t_v|$, $\varepsilon_{cv} = \varepsilon_c - \varepsilon_v$, and $\eta_{cv} = \eta_c + \eta_v$.

The spectral response (SR) $\mathcal{S}$ of the system is defined in terms of the total current I^{tot} for a given monochromatic illumination at photon energy $E_\gamma = \hbar\omega$ in the form

$$\mathcal{S}(\hbar\omega) \equiv I^{\mathrm{tot}}(\hbar\omega)/\{e\Phi_0^\gamma(\hbar\omega)\}. \quad (29)$$

The total charge current $I^{\mathrm{tot}} = I^e + I^h$ is directly obtained from the charge-carrier currents as computed within the NEGF formalism, e.g., via

$$I^e_i = \frac{e}{\hbar}\int\frac{dE}{\pi}2\mathrm{Re}\{H_{0,ii+1}G^<_{i+1i}(E)\} \quad (30)$$

for the electron current in the conduction band between QDs at positions $\mathbf{R}_i$ and $\mathbf{R}_{i+1}$ [30]. A similar expression exists for the hole current I^h in the valence band in terms of the hole NEGF component $\mathbf{G}^>$. The total current can be compared to the photocurrent as given by the absorptance

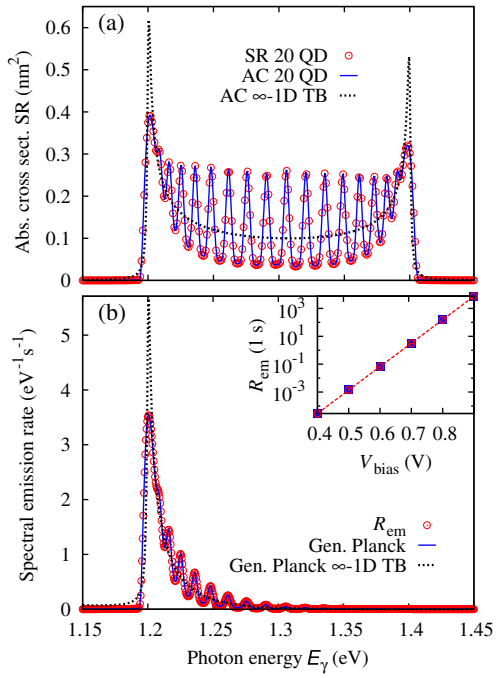

FIG. 6. (a) AC and SR of the 20-QD cell as obtained from the NEGF, in comparison with the AC of the infinite 1D TB model. (b) Spectral emission rate for the 20-QD cell at a terminal bias voltage $V_{\rm bias} \equiv \mu_R - \mu_L = 0.6$ V as derived from the NEGF formalism (empty dots) as well as from the generalized Planck law using the NEGF absorption (solid line) or the infinite 1D TB model (dotted line). The inset shows the integrated emission rate as a function of $V_{\rm bias}$, with open symbols for the values given by the current expression (30) and filled squares for the values obtained from the global emission rate (33).

and the photon flux via the spectral relation for the generation current:

$$I_{\mathcal{A}}(\hbar\omega) = e\sum_{\eta}\Phi^{\gamma}_{0\eta}(\hbar\omega)\mathcal{A}_{\eta}(\hbar\omega) \equiv e\mathcal{R}_{\rm abs,net}(\hbar\omega). \tag{31}$$

The extraction efficiency for the photogenerated charge carriers is then given by the ratio $\eta_{\rm ext} = I^{\rm tot}/I_{\mathcal{A}}$. In the situation displayed in Fig. 6(a), the SR equals the absorption cross section $\mathcal{A}$, which corresponds to unit extraction efficiency $\eta_{\rm ext} = 1$, i.e., $I^{\rm tot} = I_{\mathcal{A}}$.

D. Radiative recombination and dark current

At the radiative limit, the dark-current-voltage characteristics of the selectively contacted QD array solar cell is determined by the current due to radiative recombination of charge carriers injected at the contacts. For the description of the associated spontaneous-emission process, consideration of the photon Green's function of the entire system is required to include all the optical modes with finite coupling. Under the assumption of an optically homogeneous medium, use of the free-field photon propagator results in the SE [29]

$$\Sigma^{e\gamma-sp,\lessgtr}_{ij}(E) \approx \frac{\mu_0 n_r}{\pi c_0}\bar{\mathcal{M}}^{e\gamma}_i\bar{\mathcal{M}}^{e\gamma}_j\int_0^\infty \frac{dE'}{2\pi\hbar}E' G^{\lessgtr}_{ij}(E\pm E'), \tag{32}$$

where $\bar{\mathcal{M}}$'s are the polarization-averaged coupling elements. In terms of the photon SE, the polarization-averaged spectral emission rate of the QD array acquires the form

$$\bar{\mathcal{R}}_{\rm em}(\hbar\omega) = \frac{n_r\omega}{2\pi^2\hbar c_0}\sum_{i,j}{\rm Re}\{i\bar{\Pi}^{<}_{ji}(\hbar\omega)\}, \tag{33}$$

which is obtained by using $\Sigma^{e\gamma-sp}$ in the expression for the emission rate, in analogy to Eq. (18). For valid assumption of a *global* quasiequilibrium, the *Kubo-Martin-Schwinger* relation between the components of the polarization function [31,32], $\mathcal{P}^{<}(\hbar\omega) = \mathcal{P}^{>}(\hbar\omega)e^{-\beta(\hbar\omega-\mu_{cv})}$, with $\beta = (k_BT)^{-1}$ and $\mu_{cv} = \mu_c - \mu_v$ the quasi-Fermi-level splitting (QFLS), can be used in Eqs. (19) and (33) to derive the generalized Planck law [33] via the connection [34]

$$\bar{\mathcal{R}}_{\rm em}(\hbar\omega) = \bar{\mathcal{A}}(\hbar\omega)\frac{(\hbar\omega)^2 n_r^2}{\pi^2\hbar^3 c_0^2}\{e^{\beta(\hbar\omega-\mu_{cv})}-1\}^{-1}. \tag{34}$$

To obtain the QFLS, the individual QFL μ_c and μ_v of electrons and holes in conduction and valence bands need to be determined. They can be defined via the carrier density and the spectral function (23) under the assumption of quasiequilibrium conditions. An energy-independent value of the QFL is extracted from the density determined via energy integration of $G^{\lessgtr}$. Figure 6(b) shows the comparison of the electroluminescence spectra as obtained from the NEGF via the above formalism for the 20-QD system at a terminal bias voltage $V_{\rm bias} = \mu_R - \mu_L = 0.6$ V (empty dots) with the generalized Planck emission for AC determined either via NEGF for the same finite system (solid line) or for the infinite TB chain (dotted line). The effective emission edge of the 20-QD cell is close to that of the infinite 1D TB model, as expected from the convergence of the spectral width of the JDOS seen in Fig. 6(a). The linear increase of the QFLS with $V_{\rm bias}$ results in an exponential growth of the emission rate, as displayed in the inset of Fig. 6(b).

E. Carrier extraction efficiency

Reduced carrier extraction efficiencies ($\eta_{\rm ext} < 1$) occur when the charge recombination rate reaches a level that is comparable to the extraction rate. In the NEGF formalism, these two competing rates are obtained from expressions similar to Eq. (18), using the out-scattering component of either: the self-energy of the recombination process [i.e., of the spontaneous emission (32) in the case of the radiative

limit] or the contact self-energy (9), since the total current equals the sum of electron and hole terminal currents,

$$I_B = q \int \frac{dE}{2\pi\hbar} \mathrm{tr}[\Sigma^{>B}(E)\mathbf{G}^{<}(E) - \Sigma^{<B}(E)\mathbf{G}^{>}(E)], \quad (35)$$

where the integration is over both conduction and valence bands. Since the total current is constant over the whole device, $I_B = I^{\mathrm{tot}}$ holds. The radiative and extraction lifetimes $\tau_{\mathrm{rad,ext}}$ are directly proportional to the imaginary part of the corresponding self-energy, i.e., to the broadening function

$$\Gamma_x \equiv i(\Sigma_x^{>} - \Sigma_x^{<}) = i(\Sigma_x^{R} - \Sigma_x^{R\dagger}) \quad (36)$$

via $\tau_x = \hbar/\Gamma_x$ ($x = \mathrm{rad}, \mathrm{ext}$). Hence, subunit carrier extraction efficiencies can result from either low rates of escape into contacts or increased rates of recombination within the absorber. The relation between carrier recombination and extraction is reflected in the evolution during the self-consistency iteration of Green's functions and self-energies of the recombination rate or terminal current towards the steady-state generation rate or current, respectively. This evolution is shown in Fig. 7 for the two extreme cases of photoluminescence $\eta_{\mathrm{ext}} = 0$ [Fig. 7(a)], i.e., vanishing carrier extraction due to closed contacts ($V_c = V_v \equiv V_B = 0$), assuming a recombination lifetime $\tau_r \approx 1$ ps [35] and Fig. 7(b) perfect photocarrier extraction ($\eta_{\mathrm{ext}} = 1$) for large contact coupling ($V_{cR} = V_{vL} \equiv V_B = 0.15$ eV) and long carrier lifetime $\tau_r = 1$ s. In the intermediate case, Fig. 7(c), smaller values of contact coupling ($V_{cR} = V_{vL} \equiv V_B = 0.02$ eV) and radiative lifetime ($\tau_r \approx 10$ ps) lead to an incomplete carrier extraction ($0 < \eta_{\mathrm{ext}} < 1$) due to recombination losses. In all cases, an interdot coupling of $|t_{c,v}| = 0.03, 0.02$ eV is used, and the rates are normalized to the absorption rate $R_{\mathrm{abs}} = \Phi_0 \mathcal{A}$.

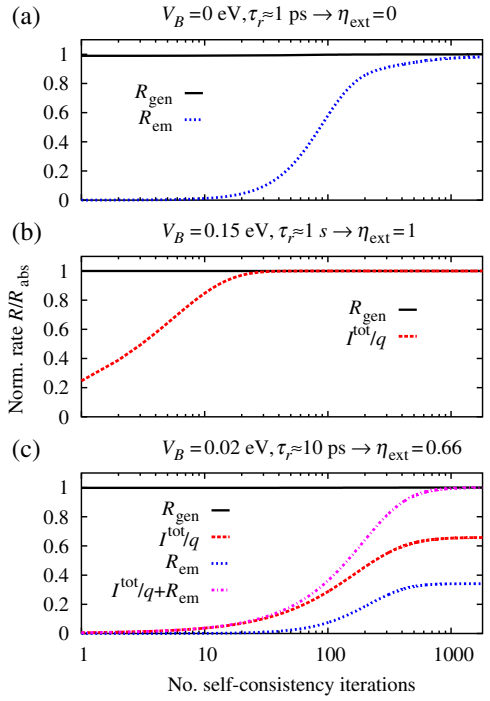

FIG. 7. Evolution during the NEGF self-consistency iteration of the energy-integrated rates for charge-carrier generation (R_{gen}), radiative recombination (R_{em}), and extraction (I^{tot}/q) normalized to the absorption rate given by the incident photon flux and the absorptance, for different regimes of operation. (a) Optical extraction only ($\rightarrow \eta_{\mathrm{ext}} = 0$), i.e., photoluminescence at closed contacts ($V_c = V_v \equiv V_B = 0$) and a recombination lifetime $\tau_r \approx 1$ ps. (b) Unit carrier extraction at electrodes ($\rightarrow \eta_{\mathrm{ext}} = 1$) due to strong dot-contact coupling $V_{cR} = V_{vL} \equiv V_B = 0.15$ eV and long recombination lifetime $\tau_r \approx 1$ s. (c) Incomplete carrier extraction ($\rightarrow 0 < \eta_{\mathrm{ext}} < 1$) for recombination lifetimes ($\tau_r \approx 10$ ps) comparable to the escape time at finite but low contact coupling $V_{cR} = V_{vL} \equiv V_B = 0.02$ eV. In all cases, an interdot coupling of $|t_{c,v}| = 0.03, 0.02$ eV is used.

III. NUMERICAL RESULTS AND DISCUSSION

On the basis of this general analysis, the specific impact of the dot-contact and interdot coupling on the density of states, spectral response, and radiative recombination characteristics can now be discussed. This is first done

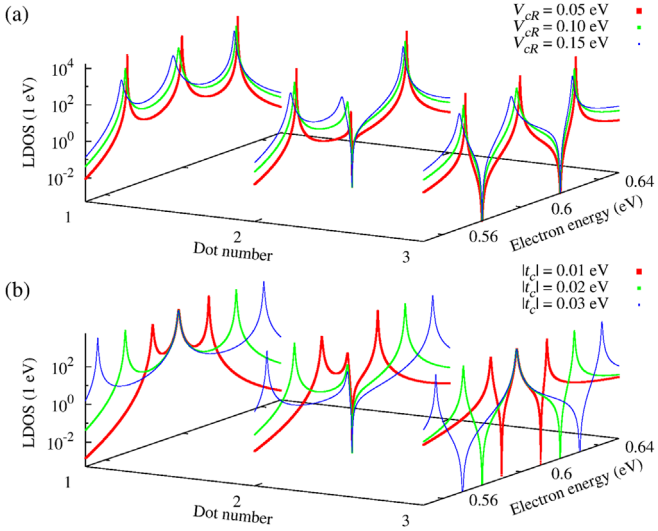

FIG. 8. Local density of electron states of a right-contacted three-QD system for varying values (a) of the contact coupling V_{cR} at fixed interdot coupling $|t_c| = 0.02$ eV and (b) of the interdot coupling $|t_c|$ at fixed contact coupling $V_{cR} = 0.1$ eV. The LDOS far from the contact acquires a regular form with peak multiplicity determined by the number of QDs. The spectral shape of the LDOS in the direct vicinity of the contact exhibits the asymmetric Fano-type signatures of the coupling of a discrete level system to the continuum of states in the bulk electrode. The effects of the contact coupling are a level broadening and a redshift that both increase with the coupling strength V_{cR}. The energy separation of the resonances, on the other hand, is directly proportional to the interdot coupling $|t_c|$.

for the situation in which photocarrier extraction is much faster than recombination ($\eta_{\text{ext}} \to 1$) and then for situations where carrier extraction competes with radiative recombination ($\eta_{\text{ext}} < 1$). All the results under illumination are obtained assuming a monochromatic spectrum with $E_\gamma = 1.3$ eV at an intensity of $I_\gamma = 10\ \text{kW/m}^2$ and normal incidence ($A_\eta = A_0 \delta_{\eta,x}$). The corresponding momentum matrix element is approximated via $p^x_{cv} \approx \bar{p}_{cv} = \sqrt{p^2_{cv}/3} = \sqrt{E_P m_0/6}$, with the Kane energy $E_P = 2.6$ eV [20].

A. $\eta_{\text{ext}} \to 1$

Figure 8(a) displays the LDOS of electrons in a three-QD chain contacted from the right, at a fixed interdot coupling $|t_c| = 0.02$ eV and varying dot-contact coupling strength. The hybridization of the discrete QD levels with the continuum of bulk electrode states introduces Fano-type asymmetric features close to the contact, which gradually disappear with increasing distance from the electrode. The main effect of the presence of this contact is the broadening of the LDOS, especially in the vicinity of the electrode, where the band width can be strongly increased as shown in Fig. 2. Since the electrode self-energy exhibits a real part, the magnitude of V_{cR} affects not only this broadening but also induces a shift in the resonance peaks. As can be inferred from Fig. 8(b), where the contact coupling is fixed at a value of $V_{cR} = 0.1$ eV, the interdot coupling acts on the LDOS mainly via the direct relation to the miniband width. These effects of the coupling parameters are retained in larger arrays. Figure 9 shows the electronic LDOS of a 20-QD array resolved on the individual dot sites for a fixed interdot coupling $|t_c| = 0.03$ eV and different values of the dot-contact coupling. At weak coupling of $V_B = 0.05$ eV, the LDOS is symmetric with respect to both the contacts and the central level energy; i.e., it is not affected by the coupling to the electrode states. For an intermediate coupling of $V_B = 0.15$ eV, there are visible contact-induced effects such as broadening and a shifting of the DOS weight towards the lower-energy band edge on QD sites in the vicinity of the contact. Finally, for strong coupling of $V_B = 0.3$ eV, localized surface states appear below the lower band edge at the open contact, while the LDOS remains almost unaffected in the vicinity of the closed contact.

The dependence of absorption and emission characteristics on the dot-contact and the interdot coupling are displayed in Figs. 10 and 11, respectively. In Fig. 10(a), the

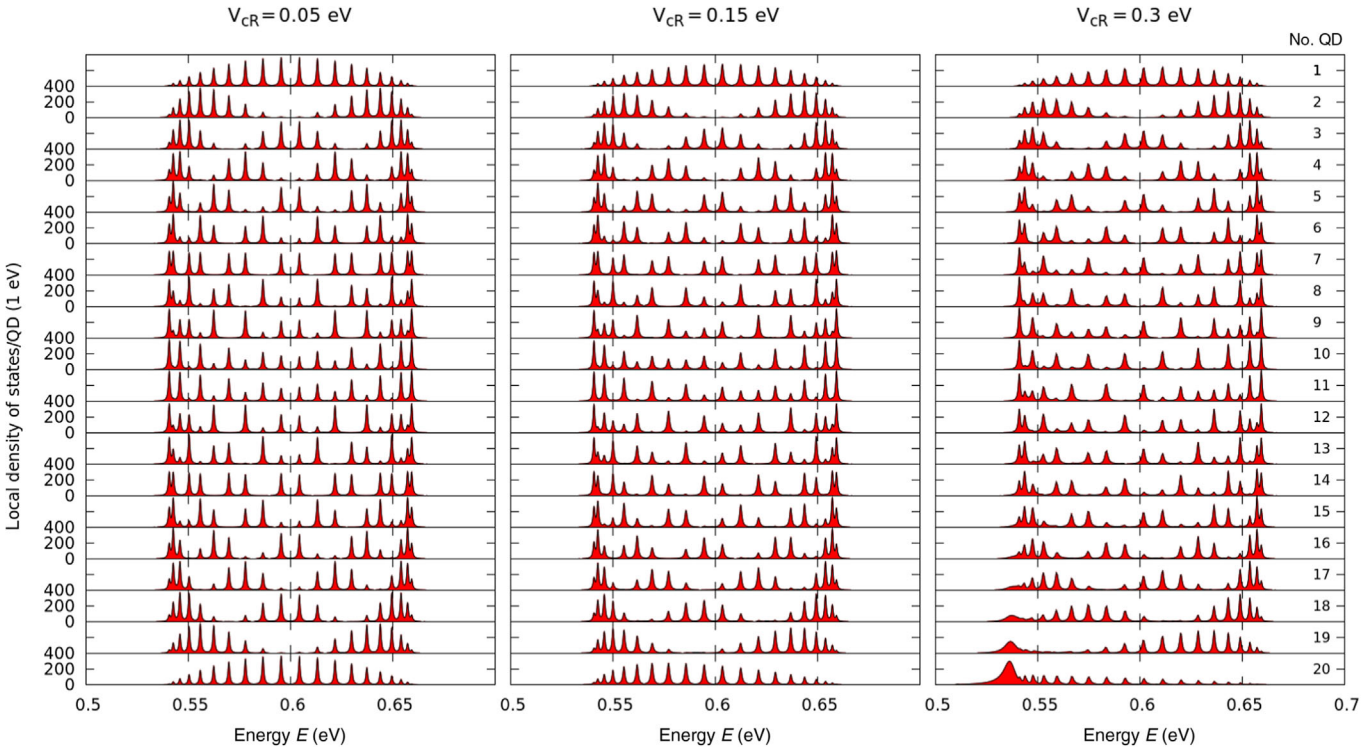

FIG. 9. LDOS of a selectively contacted 20-QD array resolved on the individual dot sites and displayed for different values of the contact coupling $V_{cR} = 0.05, 0.15, 0.3$ eV, at a fixed interdot coupling of $|t_c| = 0.03$ eV. While for the weakest coupling, the DOS is almost symmetric both along the array and with respect to the central level energy at $\varepsilon_c = 0.6$ eV, the asymmetry induced to the real part of the contact self-energy is already visible at intermediate coupling and results in the formation of a bound interface state below the low-energy edge of the miniband at the contact layer. In addition, there is the broadening of the DOS increasing with coupling strength, which originates in the imaginary part of the contact self-energy.

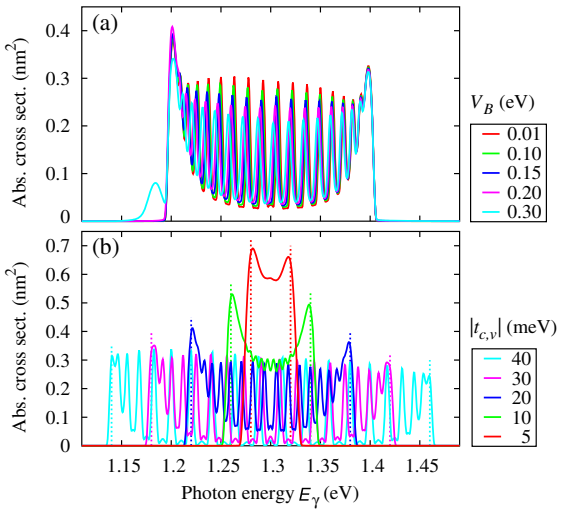

FIG. 10. The absorption cross section for the 20-QD cell is presented in (a) for various values of dot-contact couplings $V_{cR} = V_{vL} \equiv V_B$ at $|t_{c,v}| = 0.03, 0.02$ eV and in (b) for different interdot coupling parameters $t = |t_c| = |t_v|$ at $V_{cR} = V_{vL} \equiv V_B = 0.05$ eV (dashed lines indicate band width of 1D TB chain).

spread in energy of the individual dot contributions to the absorption cross section is determined by the contact-induced broadening. The width of the AC, on the other hand, is determined by the interdot coupling in analogy to the DOS of the individual bands, as shown in Fig. 10(b). It converges with an increasing number of dots to that of the single-orbital TB chain (dashed lines). Figures 11(a) and 11(b) show the impact of contact and interdot coupling strength on the levels of radiative dark-current generation.

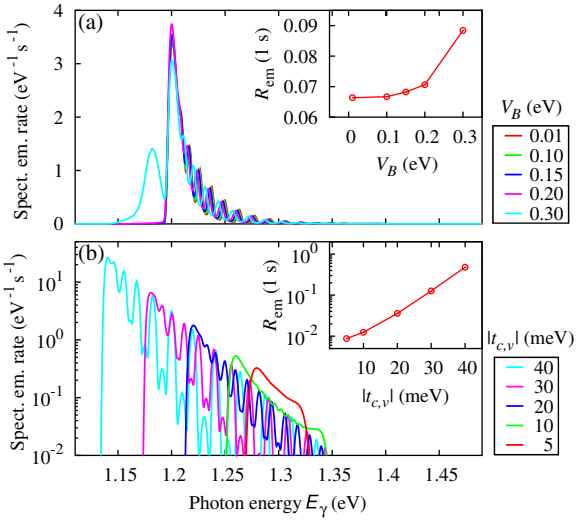

FIG. 11. Spectral emission rate for the 20 QDs at a terminal bias voltage $V_{\text{bias}} = 0.6$ V in (a) for different dot-contact couplings and in (b) for different interdot couplings. The inset displays the corresponding variation of the energy-integrated emission rate.

Up to moderate coupling strength ($V_B \leq 0.2$ eV), the effective gap is only marginally affected by the contact coupling, and there is just a slight increase of the dark current with stronger contact hybridization due to the contact-induced smearing and renormalization (i.e., red-shifting) of the emission edge, as displayed in Fig. 11(a). At larger V_B, the surface states modify the optical spectra, most pronouncedly that of the emission, with considerable increase in the integrated emission rate. On the other hand, Fig. 11(b) reveals the exponential increase of the recombination with interdot coupling strength due to the linear decrease of effective band gap $\varepsilon_{cv}^{\text{eff}} = \varepsilon_{cv}^{0} - 2(|t_c| + |t_v|)$, i.e., the decrease of the energy of the dominant contribution to the overall emission process.

B. $\eta_{\text{ext}} < 1$

In the following, the carrier lifetime is limited to a level comparable to that of the extraction by the presence of effective charge-carrier recombination processes, which can result in subunit extraction efficiency, corresponding to recombination prior to extraction. The NEGF formalism used for the evaluation of extraction efficiency is based on a steady-state picture of carrier transport, where the different lifetimes do not appear explicitly. However, as outlined in Sec. II E and illustrated in Fig. 7, the time evolution of the interacting system is mimicked by the self-consistency iteration of carrier Green's functions and interaction self-energies towards the stationary state.

In Fig. 12, the convergence of the terminal current normalized to the absorption rate is shown for a 20-QD

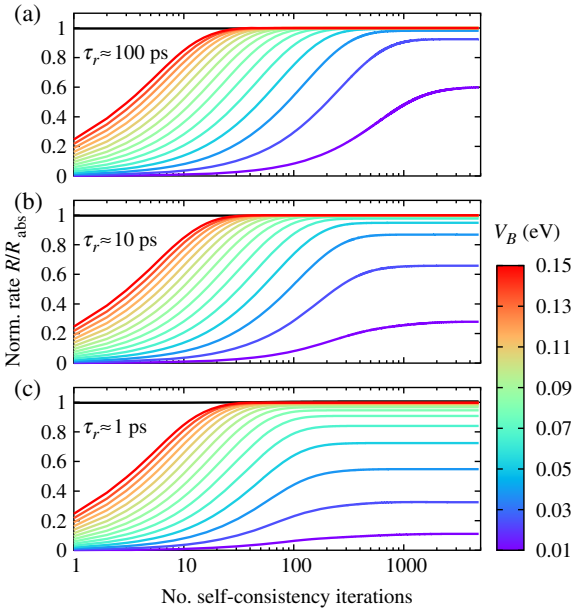

FIG. 12. Convergence of the terminal current in the NEGF self-consistency iteration for different values of contact coupling V_B, fixed interdot coupling $|t_{c,v}| = 0.03, 0.02$ eV and recombination lifetimes of (a) $\tau_r \approx 100$ ps, (b) $\tau_r \approx 10$ ps, and (c) $\tau_r \approx 1$ ps.

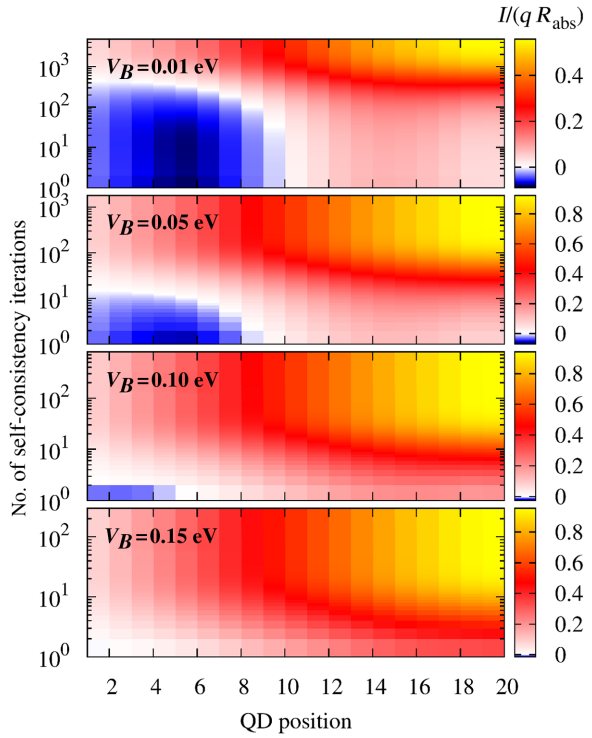

FIG. 13. Convergence of the local current resolved on individual dot position and for different values of the contact coupling V_B, revealing a pronounced dependence of photocurrent rectification on the size of the coupling, which is related to the extraction rate as well as to reflection of photogenerated charge carriers.

system with $|t_{c,v}| = 0.03, 0.02$ eV, $V_B \in [0.01, 0.15]$ eV [36], and an effective recombination lifetime of $\tau_r \approx 100$ ps [Fig. 12(a)], $\tau_r \approx 10$ ps [Fig. 12(b)], and $\tau_r \approx 1$ ps [Fig. 12(c)]. For large dot-contact coupling, unit extraction efficiency is reached after a small number of iterations and independent of lifetime. The smaller the lifetime, the larger the critical contact coupling at which the system converges to a stationary state with subunit extraction efficiency, and the sooner this convergence is achieved. For a qualitative explanation of this behavior, the convergence of the current is displayed in Fig. 13 in spatial resolution. This reveals a photocurrent rectification process whose speed depends on the size of the dot-contact coupling: the larger the coupling, the larger the electron "sink" and the less reflection at the open contact, i.e., the smaller the negative current contributions corresponding to the fraction of charge carriers traveling towards the "wrong" contact.

The convergence behavior of the terminal current with respect to varying interdot coupling $|t_{c,v}| \in [5, 50]$ meV for fixed contact coupling $V_B = 0.05$ eV and the same values for recombination lifetimes as in Fig. 12 is displayed in Fig. 14. As compared to the effect of varying V_B, the spread induced by varying $t_{c,v}$ is less pronounced, and at a recombination lifetime of $\tau_r \approx 100$ ps, unit extraction

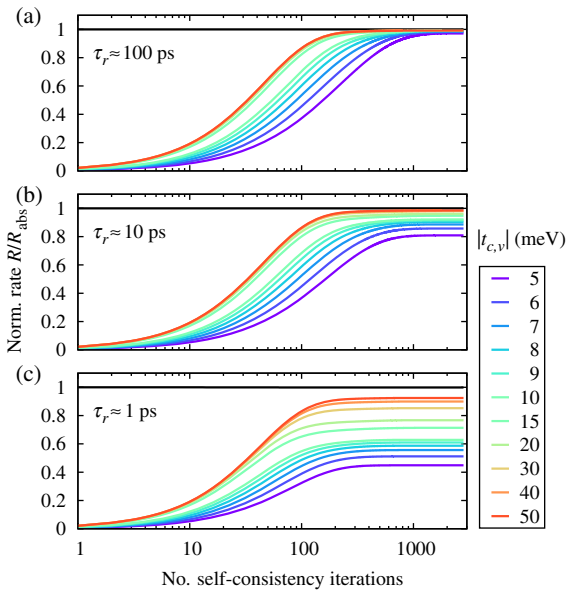

FIG. 14. Convergence of the terminal current in the NEGF self-consistency iteration for different values of interdot coupling $|t_{c,v}|$, fixed contact coupling $V_B = 0.05$ eV, and recombination lifetimes of (a) $\tau_r \approx 100$ ps, (b) $\tau_r \approx 10$ ps, and (c) $\tau_r \approx 1$ ps.

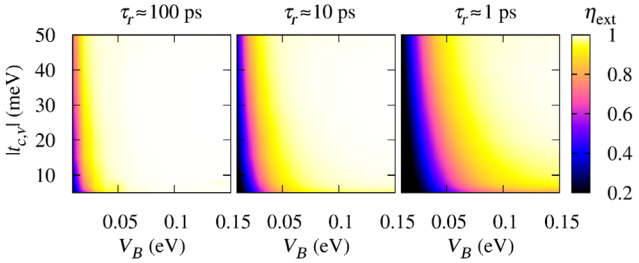

FIG. 15. Carrier extraction efficiency for configurations of interdot coupling $|t_{c,v}| \in [5, 50]$ meV and dot-contact coupling $V_B \in [0.01, 0.15]$ eV and different recombination lifetimes. At all lifetimes, the predominant effect on the extraction efficiency originates in the dot-contact coupling.

efficiency is achieved for all values of the interdot coupling considered.

Finally, the photocarrier extraction efficiency is evaluated for the whole configurational parameter space $\{V_B, |t_{c,v}|\} \in [10, 150] \otimes [5, 50]$ meV, and the three different lifetimes $\tau_r \approx 100, 10, 1$ ps. The result is displayed in Fig. 15. It shows again that the dot-contact coupling value dominates at all lifetimes. For $\tau_r \approx 100$ ps, subunit photocarrier extraction efficiency occurs only for very weak dot-contact couplings, while at $\tau_r \approx 1$ ps, complete extraction may be achieved only for large values of both interdot and dot-contact coupling.

IV. CONCLUSIONS

In conclusion, we introduce and apply a customized NEGF simulation framework to provide a direct relation

between the local quantum-dot array configuration in terms of system size as well as interdot and dot-contact coupling strength, and the global photovoltaic device performance of a finite and selectively contacted QD array, mimicking a 1D QD solid. For long carrier lifetime $\tau_r \gg 100$ ps and moderate contact coupling $V_B < 0.2$ eV, the dominant effects result from the dependence of the joint density of states on the interdot coupling and the system size in terms of spectral shape, band width, and effective gap. At large contact coupling $V_B > 0.2$ eV, localized surface states form and have a sizable impact on the optical spectra. For $\tau_r < 100$ ps, where the recombination rates start to compete with the escape rates, the dot-contact coupling becomes the dominant factor for carrier extraction. At an effective carrier lifetime of 1 ps, values of contact coupling $V_B < 0.1$ eV start to limit carrier extraction at any interdot coupling strength.

The analysis, though performed here for a specific and simplified QD system, can be extended to more complex descriptions of the local electronic structure and to any kind of disorder affecting the charge-carrier transport and, hence, the extraction efficiency. The configuration-dependent results of this investigation can be generalized to more realistic 3D systems in straightforward fashion by adding a transverse dispersion to the diagonal elements of the tight-binding Hamiltonian [37], in analogy to the planar orbital basis used in atomistic tight binding [24]. Finally, disorder in QD size and spacing present in realistic systems can be considered either by a configurational average [38] or via the self-energy for a disorder potential [15].

[1] M. A. Green, Potential for low dimensional structures in photovoltaics, Mater. Sci. Eng. B **74**, 118 (2000).

[2] A. Martí, *Next Generation Photovoltaics: High Efficiency through Full Spectrum Utilization*, Series in Optics and Optoelectronics (Institute of Physics, Bristol, 2004).

[3] L. Tsakalakos, Nanostructures for photovoltaics, Mater. Sci. Eng. R **62**, 175 (2008).

[4] V. Aroutiounian, S. Petrosyan, A. Khachatryan, and K. Touryan, Quantum dot solar cells, J. Appl. Phys. **89**, 2268 (2001).

[5] A. Nozik, Quantum dot solar cells, Physica (Amsterdam) **14E**, 115 (2002).

[6] R. P. Raffaelle, S. L. Castro, A. F. Hepp, and S. G. Bailey, Quantum dot solar cells, Prog. Photovoltaics **10**, 433 (2002).

[7] A. Martí, N. López, E. Antolín, E. Cánovas, C. Stanley, C. Farmer, L. Cuadra, and A. Luque, Novel semiconductor solar cell structures: The quantum dot intermediate band solar cell, Thin Solid Films **511–512**, 638 (2006).

[8] R. Oshima, A. Takata, and Y. Okada, Strain-compensated InAs/GaNAs quantum dots for use in high-efficiency solar cells, Appl. Phys. Lett. **93**, 083111 (2008).

[9] G. Conibeer, M. Green, E.-C. Cho, D. König, Y.-H. Cho, T. Fangsuwannarak, G. Scardera, E. Pink, Y. Huang, T. Puzzer, S. Huang, D. Song, C. Flynn, S. Park, X. Hao, and D. Mansfield, Silicon quantum dot nanostructures for tandem photovoltaic cells, Thin Solid Films **516**, 6748 (2008).

[10] V. Aroutiounian, S. Petrosyan, and A. Khachatryan, Studies of the photocurrent in quantum dot solar cells by the application of a new theoretical model, Sol. Energy Mater. Sol. Cells **89**, 165 (2005).

[11] Q. Shao, A. A. Balandin, A. I. Fedoseyev, and M. Turowski, Intermediate-band solar cells based on quantum dot supracrystals, Appl. Phys. Lett. **91**, 163503 (2007).

[12] M. Gioannini, A. P. Cedola, N. D. Santo, F. Bertazzi, and F. Cappelluti, Simulation of quantum dot solar cells including carrier intersubband dynamics and transport, IEEE J. Photovoltaics **3**, 1271 (2013).

[13] U. Aeberhard, Theory and simulation of quantum photovoltaic devices based on the non-equilibrium Green's function formalism, J. Comput. Electron. **10**, 394 (2011).

[14] U. Aeberhard, Effective microscopic theory of quantum dot superlattice solar cells, Opt. Quantum Electron. **44**, 133 (2012).

[15] N. Vukmirović, Z. Ikonic, D. Indjin, and P. Harrison, Quantum transport in semiconductor quantum dot superlattices: Electron-phonon resonances and polaron effects, Phys. Rev. B **76**, 245313 (2007).

[16] A. Wacker, Semiconductor superlattices: A model system for nonlinear transport, Phys. Rep. **357**, 1 (2002).

[17] L. Keldysh, Diagram technique for nonequilibrium processes, Sov. Phys. JETP **20**, 1018 (1965).

[18] T. Frederiksen, Master's thesis, Technical University of Denmark, 2004.

[19] U. Aeberhard, R. Vaxenburg, E. Lifshitz, and S. Tomic, Fluorescence of colloidal PbSe/PbS QDs in NIR luminescent solar concentrators, Phys. Chem. Chem. Phys. **14**, 16223 (2012).

[20] A. C. Bartnik, F. W. Wise, A. Kigel, and E. Lifshitz, Electronic structure of PbSe/PbS core-shell quantum dots, Phys. Rev. B **75**, 245424 (2007).

[21] R. Vaxenburg and E. Lifshitz, Alloy and heterostructure architectures as promising tools for controlling electronic properties of semiconductor quantum dots, Phys. Rev. B **85**, 075304 (2012).

[22] C.-W. Jiang and M. A. Green, Silicon quantum dot superlattices: Modeling of energy bands, densities of states, and mobilities for silicon tandem solar cell applications, J. Appl. Phys. **99**, 114902 (2006).

[23] S. Tomić, T. S. Jones, and N. M. Harrison, Absorption characteristics of a quantum dot array induced intermediate band: Implications for solar cell design, Appl. Phys. Lett. **93**, 263105 (2008).

[24] R. Lake, G. Klimeck, R. Bowen, and D. Jovanovic, Single and multiband modelling of quantum electron transport through layered semiconductor devices, J. Appl. Phys. **81**, 7845 (1997).

[25] A perturbative approach might not always apply in QD array systems. In some cases of strong electron-phonon interaction, a polaronic picture might be more appropriate. In this paper, this description is merely used as a phenomenological but still current-conserving broadening mechanism.

[26] U. Aeberhard, Quantum-kinetic theory of steady-state photocurrent generation in thin films: Coherent versus incoherent coupling, Phys. Rev. B **89**, 115303 (2014).

[27] U. Aeberhard, Quantum-kinetic theory of photocurrent generation via direct and phonon-mediated optical transitions, Phys. Rev. B **84**, 035454 (2011).

[28] M. Pourfath and H. Kosina, Computational study of carbon-based electronics, J. Comput. Electron. **8**, 427 (2009).

[29] U. Aeberhard, Simulation of nanostructure-based and ultra-thin film solar cell devices beyond the classical picture, J. Photon. Energy **4**, 042099 (2014).

[30] R. K. Lake and R. R. Pandey, in *Handbook of Semiconductor Nanostructures*, edited by A. A. Balandin and K. L. Wang (American Scientific Publishers, Valencia, USA, 2006).

[31] M. F. Pereira and K. Henneberger, Microscopic theory for the influence of coulomb correlations in the light-emission properties of semiconductor quantum wells, Phys. Rev. B **58**, 2064 (1998).

[32] F. Richter, M. Florian, and K. Henneberger, Generalized radiation law for excited media in a nonequilibrium steady state, Phys. Rev. B **78**, 205114 (2008).

[33] P. Würfel, The chemical potential of radiation, J. Phys. C **15**, 3967 (1982).

[34] Strictly, this relation between absorption at zero bias and emission under finite QFLS is only valid if neither JDOS nor the optical matrix elements $\mathcal{M}^{eγ}$ are modified at finite bias voltage, e.g., due to a change in orbital overlap or local band bending.

[35] In order to reproduce lifetimes of recombination processes that compete with carrier extraction, the radiative recombination is enhanced by a corresponding factor in the self-energy of the spontaneous emission.

[36] The upper bound to V_B is chosen in order to exclude spurious effects of surface states.

[37] D. M. -T. Kuo, G. Y. Guo, and Y.-C. Chang, Tunneling current through a quantum dot array, Appl. Phys. Lett. **79**, 3851 (2001).

[38] I. Gómez, F. Domínguez-Adame, E. Diez, and P. Orellana, Transport in random quantum dot superlattices, J. Appl. Phys. **92**, 4486 (2002).